Creating Metal Nanostructures at Metal Surfaces Using Growth Kinetics

Harald BRUNE

Institut de Physique des Nanostructures (IPN)
Ecole Polytechnique Fédérale de Lausanne (EPFL)
Station 3, CH-1015 Lausanne, Switzerland

Contents

Abstract

We discuss the structure and size of metal islands formed by atomic-beam deposition onto single crystal metal surfaces. Most of the procedures described can straightforwardly be transferred to oxide and semiconductor substrates. We start with the preparation and stability of the smallest islands, namely single atoms. Isolated and immobile adatoms are formed by deposition at substrate temperatures where thermal diffusion is inhibited. In the ideal case this leads to statistical growth, however one often observes slight deviations caused by neighbor driven mobility. We discuss how ordered superlattices of adatoms can be stabilized by using short-range repulsive together with long-range oscillatory interactions between adsorbates. In some examples these interactions add up and become anisotropic, leading to the formation of atomic chains in-midst of atomic terraces. We discuss coarsening by Ostwald ripening or by diffusion of entire islands. Both give rise to more narrow size distributions than nucleation and growth. We show examples for efficient stress relief at steps in monolayer high islands. Finally methods are presented to create bimetallic core-shell islands. These islands are ideally suited to compare physical and chemical properties of step atoms with the ones of higher coordinated surface atoms, or to investigate the role of one-dimensional interfaces between two metals.

Keywords: epitaxy, self-assembly, superlattices, diffusion, ripening, nucleation, Ostwald ripening, statistical growth, scanning tunneling microscopy, magnetism, nanostructures

15.1. Introduction

The interest in growing large ensembles of well defined nanostructures is the investigation of their physical and chemical properties as a function of size, composition, and also coordination of the constituent atoms. Many properties are most conveniently investigated with spatially integrating techniques, requiring high densities of particles with uniform size, composition, structure, and shape. In this chapter we describe how to create ensembles of isolated, randomly spaced adatoms, well ordered adatom superlattices, compact monolayer high islands with size ranging from a few up to a few thousand atoms, and eventually bi-metallic islands where one element forms the core surrounded by a shell formed by the second element. The approach is based on kinetically controlled growth by means of molecular beam epitaxy (MBE) onto a low-index single crystal surface held at a given temperature during growth or annealed after growth. The creation of order is based on the hierarchy of activation energies of the atomic and molecular displacements, and on the variation of the binding energy as a function of lateral position on the surface caused by interactions between neighboring adsorbates. For a more general discussion of nucleation on homogeneous substrates, and of nucleation of ordered island superlattices the reader is referred to the literature (Michely and Krug, 2004; Brune, 1998, 2006; Evans et al., 2006).

15.2. Atom condensation onto terraces – statistical growth

In this section we discuss the first step of epitaxial growth, which is the interaction of the incoming atoms with the surface. For metals growing on metal surfaces the atoms irreversibly stick to the surface implying very efficient dissipation of the adsorption energy. At low temperatures this leads to the entire absence of surface mobility enabling one to create surfaces with large densities of isolated adatoms (which we also call monomers in this chapter). Surfaces with monomers are also the starting point for the creation of atomic superlattices and chains, to be discussed in Section 15.4, and of larger but still small islands, such as dimers, trimers, etc., as outlined in Section 15.5.

Atoms approaching a single crystal from the gas phase are attracted by the surface adsorption potential. The minimum of this potential is called adsorption energy E_{ads}, and depends on the site at which the atom condenses. The adsorption energy equals the cohesive energy E_{coh} for the special case when an atom of the same element as the substrate condenses at a kink site. Terrace adsorption energies are smaller than the ones on kinks by the adatom formation energy. On open metal surfaces, such as fcc(110), this energy is only a few tenths of an eV, whereas it is close to 1.0 eV on close-packed metal surfaces. Taking typical values for $E_{coh} = 2.95$ eV for Ag and 5.84 eV for Pt (Kittel, 1986), one derives adsorption energies ranging from 2 to 6 eV, depending on the elements and surface orientation. These energies are high and their effective dissipation leads to complete condensation at typical growth temperatures.

Adsorption energies can be measured by calorimetry, which is experimentally challenging as it requires very thin single crystal films in order to arrive at detectable temperature changes induced by the adsorption of submonolayers (Borroni-Bird et al., 1991; Stuckless
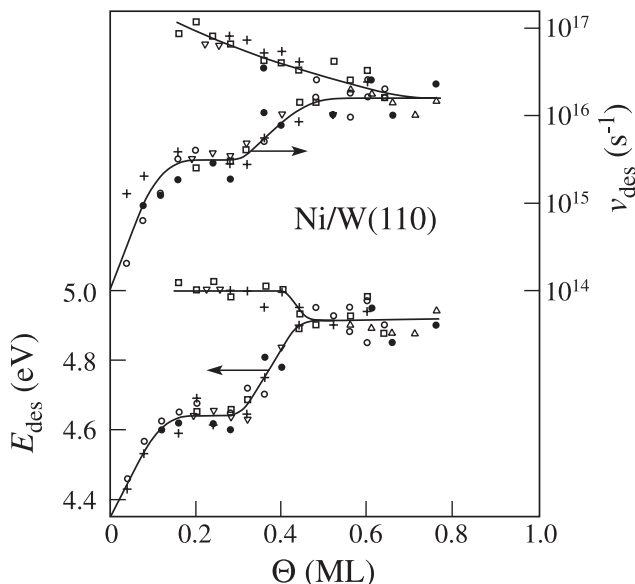
Fig. 15.1. Desorption energies $E_{des}(\Theta)$ and pre-exponential factors $\nu_{des}(\Theta)$ derived from TPD for Ni/W(110) (Kolaczkiewicz and Bauer, 1986). Upper branches correspond to atoms evaporating directly from steps, whereas the lower ones are caused by the desorption from a 2D adatom gas on the terrace.

et al., 1997; Brown et al., 1998). For systems with reversible adsorption the energies are more conveniently determined by studying the kinetics of desorption (Bauer et al., 1974; Habenschaden and Küppers, 1984). However, adsorption is only reversible for inmiscible adsorbate-substrate combinations, while it is irreversible for those heteroepitaxial systems forming bulk (Hansen, 1958) or surface alloys (Christensen et al., 1997).

One case with entirely reversible adsorption is Ni/W(110), for which Fig. 15.1 shows results obtained from temperature programmed desorption (TPD) (Kolaczkiewicz and Bauer, 1986). For coverages below $\Theta = 0.4$ ML (one monolayer, 1 ML, corresponds to one adatom per substrate surface atom) one finds two branches of the desorption energy and of its attempt frequency. The respective upper branches are caused by direct desorption from steps, while the lower ones correspond to desorption from a 2D adatom gas on the atomic terraces. This gas is present due to the continuous evaporation of step atoms onto terraces. It is further evident from Fig. 15.1 that both parameters, E_{des} and ν_{des} show a strong dependence on coverage, particularly for the lower branches.

At constant coverage, the activation energy for desorption derived from TPD equates the isosteric heat of adsorption, since for metal-on-metal systems there is no energy barrier for adsorption. Under adiabatic conditions, the isosteric heat equates the calorimetric heat of adsorption, E_{ads}, signifying altogether that $E_{des} = E_{ads}$. Desorption from steps is energetically most favorable for kink sites. Therefore the upper branch in Fig. 15.1 is related to a cohesive energy between the two elements, whereas the lower one gives access to the terrace adsorption energy. The increase of E_{des} with increasing Θ found for the lower branch is indicative of attractive adsorbate-adsorbate interactions, rendering desorp-

tion more difficult with increasing coverage. The data points are sufficiently numerous that a sensible extrapolation to the coverage limit of single adsorbed adatoms is possible. For our example one derives a terrace adatom adsorption energy of $E_{ads} = 4.36 \pm 0.03$ eV and an adatom formation energy of 0.54 ± 0.04 eV. Calorimetry has derived $E_{ads} = 3.5$ eV for submonolayer adsorption of Pb on Mo(100) (Stuckless et al., 1997). For more metal-on-metal examples the reader is referred to (Brune, 2001).

Intuition suggests that the adsorption energy might not instantaneously be dissipated, such that a fraction of it may be used for a few jumps onto sites adjacent to the impact point, at temperatures where thermal diffusion is entirely frozen. This so-called transient motion has been discussed in the literature since the early days of real-space investigations of atomic diffusion by means of field-ion microscopy (FIM) (Ehrlich, 1964; Gurney et al., 1965; Young and Schubert, 1965). While for rare gas atoms condensing on metal surfaces clear evidence of transient motion has been found by means of scanning tunneling microscopy (STM) (Xe/Pt(111) (Weiss and Eigler, 1992)), for metal atoms on metal surfaces every real space atomic scale experiment clearly excluded transient motion (for FIM results see Ehrlich and Watanabe (1991)).

We will briefly discuss these experiments. In general, transient mobility is investigated by examination of the outcome of adatom deposition onto a substrate held at low temperature in order to disable thermally activated diffusion. In the absence of transient mobility atoms come to rest at their impact site leading to what is commonly referred to as statistical growth. This implies at low coverage a statistical population of monomers on energetically non-equivalent terrace adsorption sites, and with increasing coverage an increase of the mean island size given by the statistics of deposition directly onto existing islands or onto terrace sites neighboring such islands. The presence of transient motion is detected by deviations from this behavior.

Terraces with trigonal symmetry, such as fcc(111) or hcp(0001), have two non-equivalent adsorption sites. These are the threefold-coordinated hcp- and fcc-hollows, the first an atom in the second atomic layer situated directly below, the latter not. Adatoms on these sites are imaged in FIM as triangular contours with an orientation differing by 60° between hcp and fcc-adsorption (Wang and Ehrlich, 1989). For Pt/Pt(111) adatoms were randomly distributed over hcp- and fcc-sites upon adsorption at 20 K, while annealing to 45 K promoted diffusion and led to exclusive adsorption onto fcc-sites (Gölzhäuser and Ehrlich, 1996). Hence, the hcp-site is metastable while the fcc-site is stable. The energy difference between the two sites has been estimated to be more than 60 meV, in agreement with *ab-initio*-calculations finding 180 meV more adsorption energy on the fcc site (Feibelman et al., 1994). The FIM-result implies that transient motion is absent, since any mobility would have led to a preferred population of the fcc-sites. Analog observations have been made for Ir, Re, W, and Pd adatoms on Ir(111) (Wang and Ehrlich, 1991).

STM experiments allow to discern fcc and hcp sites (Brune et al., 1990; Hofer et al., 2004) and atoms adsorbed onto these sites (Stroscio and Celotta, 2004; Yayon et al., 2006). Figure 15.2(a) shows a constant current STM image of Al(111) revealing apparent height differences between fcc- and hcp-hollows of 6 ± 1 pm. This contrast is one order of magnitude smaller than the atomic corrugation of 60 pm. Atomic resolution images of surface areas close to atomic steps of monolayer deep holes enable identification of the hollows, and one finds as expected the fcc site to have the lower apparent height (Brune et al.,
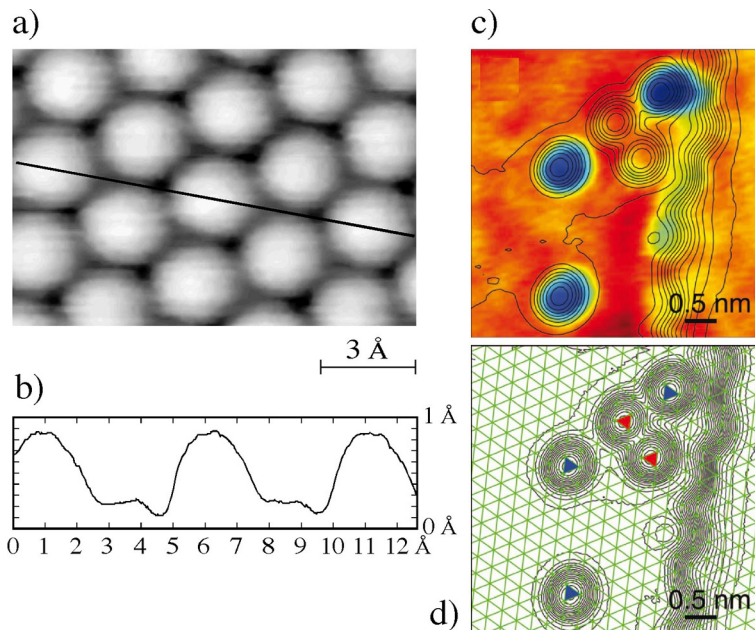
Fig. 15.2. (a) STM image showing contrast between hcp and fcc hollows on Al(111) (tunnel voltage $V_t = -20$ mV, tunnel current $I_t = 40$ nA, $T = 300$ K) (Brune et al. (1990); Hofer et al. (2004)). (b) The profile along [11$\bar{2}$] shows the fcc-hollows to be imaged 6 ± 1 pm lower than the hcp-hollows. (c) dI/dV-image of Co adatoms on Pt(111) showing the LDOS at 70 meV below E_F ($V_t = -70$ mV, $I_t = 0.2$ nA, $T = 5$ K). Co adatoms located at one of the non-equivalent hollow sites have more LDOS than the ones on the other sites. Solid lines represent constant height contours of the STM topograph. (d) The Pt(111) lattice is superimposed on the STM topograph contour lines. The triangles pointing in opposite directions represent the two hollow sites (Yayon et al., 2006).

1990). Note that the experimentally determined distance dependence of the atomic corrugation (Wintterlin et al., 1989), as well as the apparent height difference between the two hollow sites, have been reproduced by *ab-initio*-calculations taking tip-sample interactions and surface elasticity into account (Hofer et al., 2004).

Figure 15.2(c) shows Scanning Tunneling Spectroscopy (STS) measurements revealing differences in the local density of states (LDOS) between Co atoms adsorbed on the two non-equivalent hollow sites of a Pt(111) surface (Yayon et al., 2006). One species clearly has more LDOS 70 meV below E_F and appears blue in Fig. 15.2(c). There is a one-to-one correlation of the appearance of the adatoms in Fig. 15.2(c) with the orientation of the triangles marking their adsorption position with respect to the Pt(111) lattice in Fig. 15.2(d). The authors did not report occupation numbers of both sites from which conclusions on transient mobility could have been drawn, nor did they attribute whether the Co atoms appearing blue in Fig. 15.2(c) are on fcc or hcp sites.[1] We note that Co adatoms adsorbed onto fcc- and hcp-sites on Cu(111) can also be distinguished by the random telegraph noise

---

[1] For colors see the web version of this book.

caused by lateral motion of the atom when it is pulled by the tip onto the less stable hcp-site (Stroscio and Celotta, 2004).

STM studies of the island density after low temperature deposition for a given coverage yield sufficiently precise values of the mean island size s that conclusions on transient mobility can be reached (Brune et al., 1999; Michely and Krug, 2004). The mean island size expected for the square and triangular lattice symmetries for pure statistical growth can be estimated from percolation theory (Sykes and Glen, 1976; Sykes et al., 1976). Since this theory neglects deposition onto filled sites it predicts slightly smaller values than the ones found in experiment. Kinetic Monte-Carlo (KMC) simulations account for impingement onto, and subsequent downward diffusion from islands or monomers. Such simulations yield $s = 1.48$ atoms (percolation theory 1.35 atoms) without, and $s = 2.3$ atoms with transient motion over one lattice site (values for $\theta = 0.1$ ML on a triangular lattice). This difference is clearly outside the experimental error bars and has allowed to rule out transient mobility for Ag/Pt(111) (Brune et al., 1999). Similar conclusions have been drawn from STM images acquired for Ni and Au/Au(110), where transient motion was excluded based on the chain lengths and distances (Hitzke et al., 1997), and on island size distributions (Günther et al., 1997), respectively.

Transient motion has been inferred indirectly from diffraction experiments. Reflection high-energy diffraction (RHEED)-oscillations suggested 2D growth of Fe and Cu on Ag(100) at a temperature of 77 K (Egelhoff and Jacob, 1989) and rings in low-energy electron diffraction (LEED) patterns implied a mean-island spacing of ten atoms for Fe, Co, and Cu on Cu(100) at a temperature of 80 K (Nyberg et al., 1993). These observations are suggestive of transient motion since thermal diffusion is expected to be frozen at these temperatures. However, explanations of these observations without the assumption of transient motion have been proposed (Evans et al., 1990; Sanders and DePristo, 1991) such that these results cannot be considered as evidence for transient motion. The case where direct evidence of transient motion has been reported for metals-on-metals is a "knock-on" exchange process observed for Ir/Rh(100) by means of FIM (Kellogg, 1996). For this system thermally activated exchange sets in at 330 K, however, a fraction of 10% of the Ir atoms already exchanged with Rh at low T. This can be interpreted as transient vertical motion, i.e., part of E_{ads} is used to overcome the energy barrier of exchange.

In conclusion, all atomic-scale observations for metal/metal systems have so far precluded lateral transient mobility. The adsorption energy of atoms condensing from the gas phase is instantaneously transferred to the substrate bulk lattice and adatoms thermalize at their impact point. Therefore the size distributions expected from statistical growth can be realized for metal deposition at temperatures where thermally activated diffusion is frozen. At low coverages one gets an almost monodisperse distribution of single adatoms being a good starting point for the preparation of small islands with well defined sizes as we will discuss in Section 15.5.

15.3. Atom condensation close to steps and adatoms

There are several observations suggesting that the motion of an adatom towards a neighboring adatom or island is quite different from thermal diffusion of isolated adatoms. This

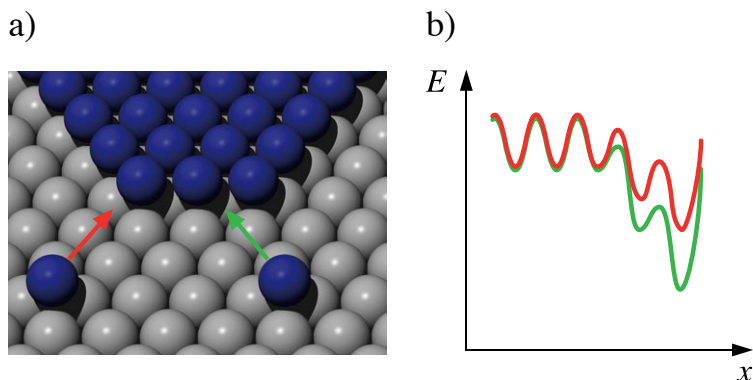a)   b)

Fig. 15.3. (a) Schematic of trajectories and (b) the corresponding variation of binding energy and diffusion barrier for adatoms approaching a step at one- and two-fold final coordination.

leads to spatial and size distributions which are slightly different from what is expected and we therefore discuss it here.

Wang and Ehrlich reported denuded zones, bare of Ir atoms, around Ir islands on Ir(111) (Wang and Ehrlich, 1993a, 1993b). In the first set of FIM experiments Ir was condensed at 20 K and its diffusion was followed subsequently after annealing periods at 105 K. Far away from the island atomic jumps could be traced in the usual way. But as soon as the lateral distance from the island was less than three nearest neighbor spacings, an atom was "funneled" in a single diffusion event toward the island (Wang and Ehrlich, 1993a). In a second experiment the same group observed that the denuded zones were somewhat narrower (two atoms wide) but that they persisted down to a temperature of 20 K, i.e., in the absence of thermally activated terrace diffusion of isolated adatoms (Wang and Ehrlich, 1993b).

These observations were interpreted as follows. Adatoms are stronger bound to ascending steps than they are on terraces. Therefore, the adatom adsorption potential becomes pulled down when approaching a step, which also reduces its corrugation for motion towards the step, see Fig. 15.3. While the first set of data can be reconciled by a 10% reduction of the diffusion barrier, the depletion at 20 K would imply a reduction of that barrier by a factor of five! This reduction seems large for attachment to a one-fold coordinated step site. At this site the binding energy is increased by approximately the dimer bond energy, amounting to 0.32 eV for this system (Wang and Ehrlich, 1990). Over a distance of two sites this reduces the terrace diffusion barrier of 0.27 eV (Wang and Ehrlich, 1989) down to 0.19 eV (red trajectory and curve in Figs. 15.3(a) and (b), respectively), which is not sufficient to explain the observed motion at 20 K.

Two- or three-fold lateral coordination to step atoms increases the binding energy in our example by approximately 0.61 and 0.76 eV, respectively (Wang and Ehrlich, 1989). This pulls the diffusion barrier down to 0.12 eV and 0.08 eV if we assume again that this increase is linearly distributed over two lattice sites (green trajectory and curve in Figs. 15.3(a) and (b), respectively). Even the lower value of 0.08 eV is still too large to explain thermal motion at 20 K. One can only rationalize the FIM observations of denuded

zones by thermal motion towards islands if much more strongly reduced barriers for the last few nearest neighbor distances are assumed. These barriers can not be attained by interactions pulling the potential linearly down over two sites. An alternative interpretation of the results would be transient motion towards the step over the smoothened potential energy surface there. Only deposition at variable low temperatures would have revealed whether and by how much the barrier is reduced and whether transient motion towards neighbors or a non-linear increase in binding energy are the origin of the denuded zones observed for Ir/Ir(111) 20 K.

In this context we note that single adatoms may also attract their neighbors and thus facilitate attachment resulting in dimer formation. Helium atom scattering experiments revealed for Pd/Ag(100) that Pd adatoms could jump over one lattice site in order to attach to their neighbors down to substrate temperatures of half the onset temperature of ordinary terrace diffusion (Vandoni et al., 1994). The activation barrier for the attachment to an other monomer is thus a factor of two smaller than the diffusion barrier for isolated adatoms. Island densities and sizes at low deposition temperatures are affected by reduced attachment barriers (Brune et al., 1999).

The experimental observations of neighbor and island driven mobility could alternatively be imagined as attraction of the atoms to neighbors or island step bottoms during their trajectory of arrival from the gas phase. However, such direct attraction to higher coordinated sites can be excluded for other systems such as Pt/Pt(111), Ag/Pt(111), Au and Ni/Au(110), which makes the explanation also unlikely for Ir/Ir(111) and Pd/Ag(100). Therefore, the currently most consistent interpretation is that metal atoms strike the surface perpendicularly, condense at the point of impact and then thermally diffuse. The adatom adsorption potential adjacent to other adatoms or islands is significantly smoothened for direction of approach by the increase in binding energy at laterally higher coordinated sites.

It remains unclear whether this smoothening suffices to explain all experimental observations of denuded zones and neighbor driven mobility reported so far. Transient motion can alternatively be considered for the last one or two jumps toward monomers or islands over the smoothened potential energy surface, however, we emphasize that transient mobility is clearly excluded for individual monomers on the corrugated adsorption potential inmidst atomic terraces.

The present discussion shows that condensation of metal atoms onto terraces is well understood, however, their condensation close to steps and other adatoms is not yet as clear, encouraging further experimental and theoretical investigation. We expect the details of the adsorption energy landscape in the vicinity of an island or a neighboring atom to become relevant at high island densities and small island sizes, i.e., at low deposition temperatures.

15.4. Superlattices and chains formed by long-range interactions

In this section we discuss the creation of lattices of equidistant metal adatoms. Short range repulsions prevent the adatoms from condensing into islands and long-range oscillatory interactions position them into the distance corresponding to the first minimum of the interaction energy. Finally we show that long- and short-range interactions can also lead to metastable monatomic chains.
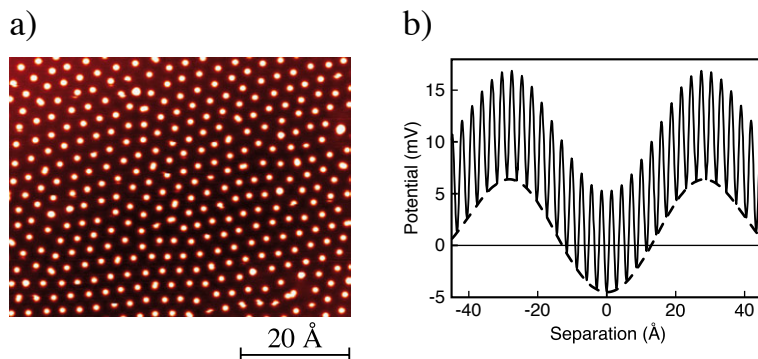
a)   b)

20 Å

Fig. 15.4. (a) STM image of well ordered Ce superlattices formed on a Ag(111) surface due to long-range ad-sorbate-adsorbate interactions mediated by surface state Friedel oscillations ($\Theta = 8 \times 10^{-3}$ ML, $T = 3.9$ K, $V_t = 0.1$ V and $I_t = 10$ pA); image courteously provided by W.D. Schneider (Silly et al., 2004a). (b) The potential energy of Ce/Ag(111) has a long-wavelength corrugation, caused by interactions of the atoms in the superlattice and a short-wavelength corrugation, which is the diffusion barrier between adjacent adsorption sites (Silly et al., 2004b).

Well ordered superlattices with a lattice constant of 32 ± 2 Å are formed spontaneously by Ce atoms on a Ag(111) surface, see Fig. 15.4(a) (Silly et al., 2004a). The best hexagonal order could be observed at 3.9 K. Increasing the temperature to 4.8 K leads to adatom diffusion around the lattice positions, equivalent to melting of the lattice. At 10 K the lattice is destroyed by irreversible nucleation of Ce islands. Figure 15.4(b) shows the long-range interaction potential of an adatom in the hexagonal lattice. This potential has been deduced by analyzing the displacements of adatoms out of their ideal superlattice positions at $T = 4.8$ K. The displacements had a Gaussian distribution with full-width at half-maximum (FWHM) of 5.8 ± 0.5 Å yielding a well depth of 4.9 ± 0.5 meV and a trapping barrier height along the [11$\bar{2}$]-equivalent direction of 11.8 ± 1.2 meV. The trapping potential is comparable with the adatom migration barrier for jumps between adjacent substrate lattice sites, which has been deduced to $E_m = 12$ meV from the hopping rate at 4.8 K under the assumption of an attempt frequency of $\nu_0 = 1 \times 10^{12}$ Hz.

The long-range interactions giving rise to the trapping barrier, and therefore to the super-lattice, are mediated by Friedel oscillations (Friedel, 1958) of an underlying surface state. In bulk Friedel mediated interactions between impurity atoms depend on the distance as $\cos(2k_F r)/r^5$ (Lau and Kohn, 1978). The $1/r^5$-decay is steeper than the monotonic $1/r^3$-decay of elastic interactions (Lau and Kohn, 1977), which therefore dominate the electronic ones from relatively short distances on. This is different for interactions mediated by Friedel oscillations in two-dimensional (2D) electron systems where the pair interaction energy between two impurities was predicted to be proportional to $\cos(2k_F r)/r^2$ (Lau and Kohn, 1978). This relatively slow decay implies that in 2D electron mediated interactions dominate elastic and dipolar ones, giving rise to oscillatory long-range interactions between impurities.

In metals nearly free 2D electron gases are realized in Shockley type surface states, e.g., on close-packed surfaces of noble metals. These states are located inside narrow band gaps
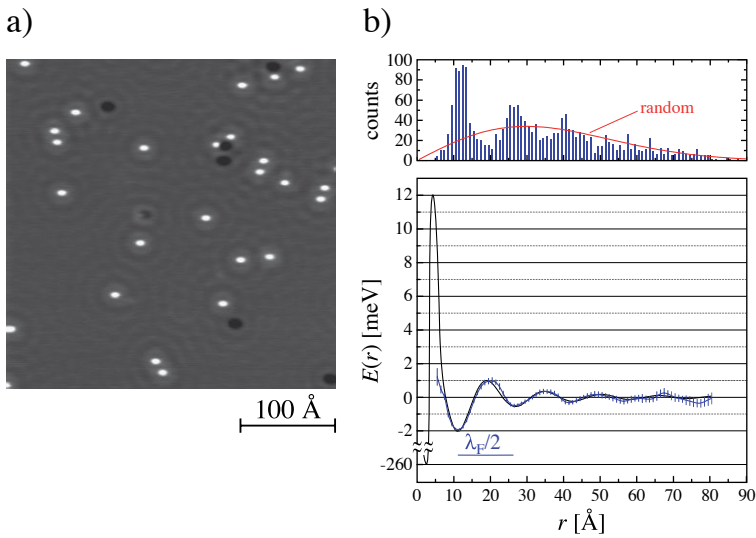
a)

b)

Fig. 15.5. (a) Surface state Friedel oscillations around Cu (bright) and impurity (black) atoms on Cu(111) ($\Theta = 1.4 \times 10^{-3}$ ML, $V_t = 100$ mV, $I_t = 0.5$ nA, $T = 13.5$ K) (Knorr et al., 2002). (b) Pair distance histogram showing a significant deviation from a random distribution (red line) and the derived pair interaction energy for large distances (Knorr et al., 2002). The thin black line shows for large distances a fit with Eq. (15.1). The repulsion at small distances has been calculated from the temperature where the superlattice collapses into islands (Venables and Brune, 2002). The dimer bond energy is taken from *ab-initio*-calculations (Ovesson et al., 2001).

in the center of the first Brillouin zone of the (111)-projected bulk band structure. This implies extremely small Fermi wave vectors. Consequently surface state Friedel oscillations have significantly larger wavelengths than those of bulk states. Friedel oscillations in surface states were first observed for Au(111) (Hasegawa and Avouris, 1993) and Cu(111) (Crommie et al., 1993a). The shortest wave vector of $k_F = 0.083$ Å^{-1}, respectively the longest period of $\lambda = \pi/k_F = 38$ Å, has been reported for Ag(111) (Jeandupeux et al., 1999). Figure 15.5(a) shows Friedel oscillations around Cu atoms on Cu(111), where $k_F = 0.21$ Å^{-1} (Crommie et al., 1993a).

Figure 15.5(a) was taken out of a sequence of images recorded at 13.5 K, where Cu adatoms readily diffuse (see videos on authors web page under gallery). Despite the fact that the atoms come quite often close to each other they remain isolated and do not form islands. This indicates the existence of short-range repulsions. For the present system, no cluster formation was observed during annealing at 16.5 K during 20 min, while almost all the monomers formed islands upon annealing at 22 K during a comparable time. From these observations the short-range repulsion has been estimated to 12 ± 2 meV (Venables and Brune, 2002). This energy can only partly be caused by surface state Friedel oscillations. Its main origins are dipole-dipole, elastic, or bulk-electron mediated interactions. Such short-range interactions have been studied by means of FIM (Ehrlich and Watanabe, 1991; Tsong, 1988) and STM (Stranick et al., 1994; Trost et al., 1996). We note here that short range repulsion is mandatory for the obser-

vation of the long range interactions and for the stabilization of adatom superlattices, since it stabilizes the adatom gas against nucleation.

Apart from to the short-range repulsion there are much weaker long-range interactions between the adatoms. The first experimental observation indicative of such interactions came from equidistant bulk segregated impurities on Cu(111) (Wahlström et al., 1998). Figure 15.5(a) shows a few adatom pairs with a preferred distance. Analysis of many such images in terms of pair distance abundances revealed significant deviations from a random distribution, see Fig. 15.5(b). These deviations can be translated into pair interaction energies. This pair potential oscillated indeed with a wave vector of $2k_F$ and agreed with the theoretically predicted asymptotic $1/r^2$-decay, see Fig. 15.5(b). The experimentally determined potential was of the form

$$E(r) = -AE_0 \left(\frac{2\sin(\delta)}{\pi} \right)^2 \frac{\sin(2qr + 2\delta)}{(qr)^2 + (qc)^2}, \tag{15.1}$$

where E_0 is the onset energy of the surface state and c a fit parameter accounting for the attenuation of the first minimum with respect to the $1/r^2$-decay. The position and amplitude of the first minimum determine the scattering phase $\delta = (0.50 \pm 0.07)\pi$ and a scattering amplitude of $A = 0.13 \pm 0.01$, which are in good agreement with the properties expected of a black-dot scatterer. The best fit is obtained with $c = 10$ Å, meaning that the first minimum is slightly attenuated with respect to $1/r^2$. This is likely due to the superposition of the surface sate mediated $E(r)$ with repulsive elastic or 3D electronic interactions at short distances. *Ab-initio*-calculations of interaction energies for Co/Cu(111) (Stepanyuk et al., 2003) yield an attenuated first minimum and are in much better agreement with experiment (Knorr et al., 2002) than the scatter model (Hyldgaard and Persson, 2000). Independent of this attenuation, the first minimum of $E(r)$ is clearly more attractive than the second one, in contrast with the curve reported in Ref. (Repp et al., 2000), where presumably many body interactions were not eliminated in the analysis. The wave vector $q = (0.20 \pm 0.01)$ Å^{-1} is in good agreement with the band structure of the Cu(111) surface state (see above). This is also true for interactions with Co atoms on Ag(111), where $q = (0.10 \pm 0.02)$ Å^{-1}, $\delta = (0.33 \pm 0.02)\pi$, $A = 0.29 \pm 0.01$, and $c = 3$ Å (Knorr et al., 2002).

Let us return to the Ce/Ag(111) system and address the question why superlattices could be formed for Ce/Ag(111), and not for the other systems studied before. From the interaction of hexagonally coordinated Ce atoms one can calculate the pair potential under the assumption of additive superposition, yielding a depth of the first minimum of $E_{min} = 0.8$ meV, and the scattering phase derived from its position is with $\delta = 0.37\pi$ in agreement with $\delta = (0.37 \pm 0.05)\pi$ derived from looking at the LDOS oscillations alone (Silly et al., 2004a).

Figure 15.6(a) shows a small hexagonally ordered island of Cu/Cu(111) (Repp et al., 2000) and Fig. 15.6(b) shows predominantly chains of equidistant atoms but there are only small patches of hexagonally close packed atomic superlattices (Knorr et al., 2002). This was also the case for Co on the same substrate, whereas Co/Ag(111) showed quasi hexagonal lattices, which were not well ordered, however (Knorr et al., 2002).

The scattering phase of Ce/Ag within the error bars is identical with the one of Co/Ag and can therefore be ruled out as dominant factor. The relative strength of the long-range interaction is for Ce/Ag(111) with $E_{min}/E_m = 1/15$ slightly larger than for Cu/Cu(111) with
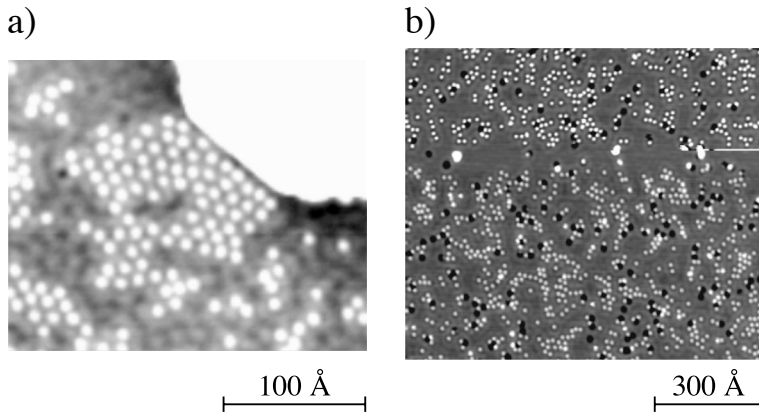
a)   b)

100 Å   300 Å

Fig. 15.6. (a) For Cu/Cu(111) the surface state mediated long-range interactions lead to small islands with hexagonal order and inter-atomic distances of 12.5 Å ($\Theta = 1 \times 10^{-2}$ ML, $T_{dep} = 15$ K, $T_{im} = 9$ K, $V_t = -0.1$ V and $I_t = 1.9$ nA) (Repp et al., 2000). (b) At slightly lower coverage there are more linear chains of equidistant atoms than hexagonally ordered areas ($\Theta = 6 \times 10^{-3}$ ML, $T = 15$ K, $V_t = -0.3$ V and $I_t = 2.0$ nA) (Knorr et al., 2002). In the upper third a tip change led to assembly of atoms into islands and a slight decrease in resolution.

$E_{min}/E_m = 1/20$ (the minimum is 2.0 meV and the diffusion barrier $E_m = 40 \pm 1$ meV (Knorr et al., 2002)). Worse is Co/Cu(111) with $E_{min}/E_m = 1.5$ meV/37 meV $= 1/25$ (minimum (Knorr et al., 2002), barrier (Tsivlin et al., 2003), and much worse Co/Ag(111) with $E_{min}/E_m = 0.8$ meV/50 meV $= 1/60$ (diffusion barrier, Knorr et al., unpublished). The relative stability toward irreversible nucleation is also slightly larger for Ce/Ag (10 K/12 meV) compared with Cu/Cu (22 K/40 meV). This enables one for Ce/Ag to reach higher relative temperatures bringing the system closer to the total energy minimum. Note, however, that temperature also creates disorder; in the case of Ce/Ag one can even melt the dilute solid before it collapses into an island (Silly et al., 2004a).

Coverage is a very important factor determining order besides the considerations on relative interaction energies, diffusion and attachment barriers. It has been reported that the lattice can be compressed from $d_{nn} = 32$ Å down to 22 Å by increasing the coverage from 1.0 to 2.0×10^{-2} ML (Silly et al., 2004b). Once a germ of a hexagonal lattice is formed, the interactions add up and the lattice orders in a self-amplifying way. The ideal coverage for Cu and Co/Cu(111) is $(d_{nn,Cu}/d_{nn,sl})^2 = (2.55/12.5)^2 = 0.04$ ML. This discussion explains why former attempts to create superlattices were unsuccessful. On Fig. 4(a) of Knorr et al. (2002) there was too little coverage, 2.1×10^{-2} ML, and on Fig. 4(b) of Knorr et al. (2002) there was the right coverage, but Co/Ag(111) is a system with too shallow $E(r)$-minimum compared with the diffusion barrier.

The fact that repulsive adsorbate-adsorbate interactions sum up may favor attachment to the ends of elongated structures and not to their sides. In the extreme case this leads to the formation of straight 1D chains, as was fist observed by means of FIM for interactions of intermediate range (Koh and Ehrlich, 2001). Ir atoms were reported to diffuse at some distance along Ir chains on W(110), and attach exclusively to their ends, see Figs. 15.7(a) and (b).
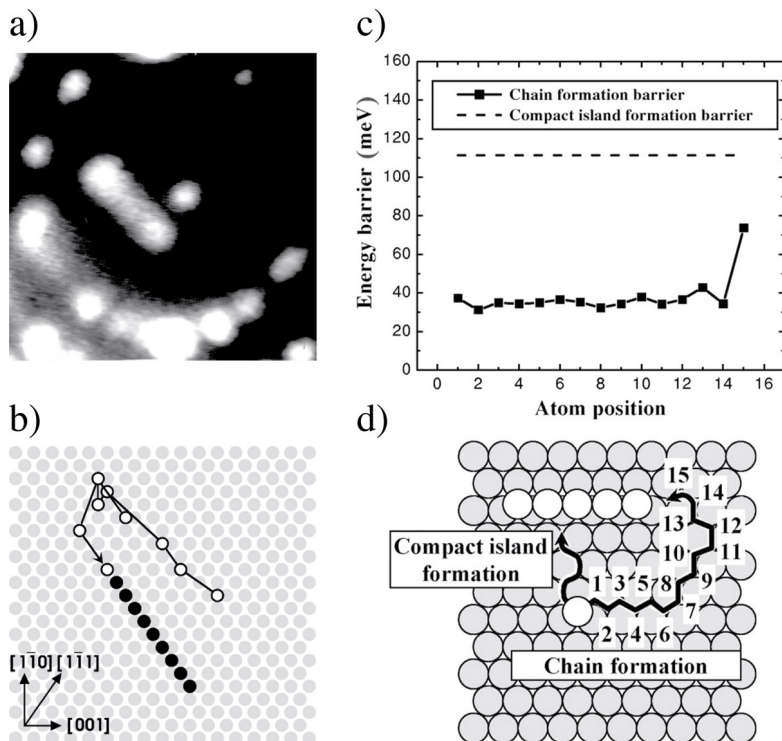
a)

c)

b)

d)

Fig. 15.7. (a) FIM image of a monatomic Ir-chain with one Ir atom close by. (b) The trajectory (350 K, 5 s) shows that the Ir atom attaches to the chain end and avoids approaching the chain from the side (Koh and Ehrlich, 2001). (c) Atomistic calculations, based on the pair interaction potential calculated with *ab-initio*-methods, show that Co chains on Cu(111) have an attachment barrier of 110 meV for Co atoms coming from the side, whereas attachment to the end has only a slightly higher barrier than terrace diffusion along the chain (Stepanyuk et al., 2003).

Calculations for Ag on compressively strained Ag(111) and Cu/Cu(111) reported strongly anisotropic repulsive barriers around elongated islands (dimers, linear trimers) favoring attachment to their ends (Fichthorn et al., 2003). Similar phenomena hold for the long-range interactions. For a chain of Co atoms sitting on the distance favored by the long-range interactions on Cu(111), the individual interactions were shown to add up leading to an attachment barrier of 60 meV for Co atoms approaching perpendicular to the chain, whereas for attachment to the chain ends there was no additional barrier than the one for terrace diffusion of 37 meV (Stepanyuk et al., 2003). This is in agreement with the preferred formation of linear structures over compact ones, observed in low coverage experiments for Cu and Co on Cu(111) (Knorr et al., 2002; Stepanyuk et al., 2003) and for Ce/Ag(111) (Silly et al., 2004b). Figures 15.7(c) and (d) show calculations for Co atoms arranged in a close packed chain on Cu(111) (Stepanyuk et al., 2003). Diffusion along the chain has a barrier of 35–40 meV, comparable to diffusion on the free terrace. Perpendicular approach of the chain by an atom costs 110 meV, while attachment to its end has a barrier of only 80 meV.

A very helpful test of ideas on the formation mechanism of certain patterns can be derived from *ab-initio*-calculations of short- and long-range interactions fed into kinetic Monte-Carlo (KMC) simulations. Recent calculations of the long-range interactions of 3*d* elements on Cu(111) predict particular superlattice stability for a number of elements, most spectacularly for Ti (Stepanyuk et al., 2004). Calculation of the diffusion barriers for these systems will enable realistic KMC simulations of the kinetics of superlattice formation and stability and stimulate new experiments. Combined *ab-initio*-KMC simulations showed that the standing LDOS waves inside circular quantum corals (Crommie et al., 1993b) are enable to create concentric Co adatom rings on Cu(111) (Stepanyuk et al., 2006).

Short and long-range repulsions have a strong influence on island densities and size distributions (Bogicevic et al., 2000; Fichthorn and Scheffler, 2000). Short-range repulsions delay nucleation to higher monomer coverage and therefore lead to modified density scaling (Ovesson et al., 2001; Venables and Brune, 2002). This partly explains small diffusion prefactors that have formerly been deduced from analyzing nucleation experiments, not knowing yet about the short-range repulsions between metal adatoms (Brune et al., 1995; Brune, 1998; Fischer et al., 1999; Barth et al., 2000). Interactions of intermediate range can add up and give rise to very high almost isotropic repulsive barriers around compact clusters. This has again consequences for the density scaling (Fichthorn et al., 2002) and favors small islands with more narrow distributions of sizes and spacings than the ones obtained without interactions (Fichthorn et al., 2003). We finally note that atomic superlattices with smaller lattice constant than the surface state Friedel-oscillation mediated ones may be stabilized by dipolar interactions of relatively short range. The most prominent examples for such interactions are alkali metals on metal surfaces. A phase transition from a dilute liquid into a well ordered solid has been reported for Cs/Ag/Si(111)-($\sqrt{3} \times \sqrt{3}$) (Liu et al., 2005).

The example of Ce/Ag demonstrates that the surface state electron mediated adsorbate-adsorbate interactions can be used for the creation of ordered atomic and possibly molecular superlattices. The lattice constant can be adjusted by the surface state band structure. Straight monatomic chains may be formed by additive adatom-adatom interactions. The nearest neighbor distance in these chains may vary from substrate to superlattice nearest neighbor distance.

15.5. Ostwald ripening

Many nanoscale surface structures are metastable. Therefore it is important to know on what time scale material rearranges and whether these processes can also be used for modifying nanostructures on surfaces in a desired way. Ostwald ripening (Ostwald, 1900) is the coarsening of an ensemble of differently sized clusters, driven by minimization of the overall cluster surface. The clusters evaporate atoms from their surface which diffuse in a surrounding medium (solid, liquid, gas) and condense either back to the same or to other clusters. Through the availability of surface microscopy at the atomic level this phenomenon has received considerable attention in two dimensions (Röder et al., 1993; Theis et al., 1995). The continuum theory of Ostwald ripening (Lifshitz and Slyozov, 1961; Wagner, 1961) has been applied to surfaces (Chakraverty, 1967; Wynblatt and Gjostein,

1975) which leads to the following expression for the evolution of the area A of an island with radius r

$$A(t, T) = -\beta\big(\rho(r) - \rho_{\text{eq}}(r)\big), \tag{15.2}$$

where $\rho(r)$ is the adatom density next to the island perimeter. The equilibrium adatom density required to maintain this island at steady size is given by $\rho_{\text{eq}}(r) = \rho_\infty \exp(\gamma/k_B T n r)$ and derived from the Gibbs–Thomson relation for circular islands with isotropic surface tension γ. The difference between these densities is the driving force of ripening. The rate β is composed of step edge evaporation, terrace diffusion, and condensation barriers and the corresponding pre-exponential factors. In many metal-on-metal systems there is no barrier for incorporation of atoms into ascending steps and Eq. (15.2) takes the form

$$A(t, T) = -\frac{2\pi D\rho_\infty}{n \ln(R/r)}\big(e^{\gamma/k_B T n r} - 1\big). \tag{15.3}$$

The diffusion constant D includes the evaporation barrier, n is the density of substrate atoms, and R the radius from the island center where ρ takes on ρ_∞. For $r \gg \gamma/k_B T n$ it suffices to keep the leading terms in the exponential series. Neglecting the size dependence in the prefactor of Eq. (15.3), one readily derives $r(t) \propto -t^x$ with $x = 1/3$. STM inspection of the island decay at 300 K for Ag/Ag(111) led to $x = 0.27 \pm 0.05$ from analysis of 20 islands (Morgenstern et al., 1996). This somewhat smaller value is attributed to the islands being small compared with the limit where a simple power law is justified. With an upper bound of $\gamma = 0.2$ eV/atom for the line tension one obtains unity in the exponent of Eq. (15.3) for $r = 3$ nm.

Attachment barriers can be introduced using a step incorporation coefficient κ (1 for attachment without barrier and 0 for infinite barrier) yielding the following expression for $r \gg \gamma/k_B T n$ (Hannon et al., 1997)

$$A(t, T) = -\frac{2\pi D\rho_\infty \gamma}{n^2 k_B T} \frac{1}{\ln(R/r) + a/\kappa r}\left(\frac{1}{r_c} - \frac{1}{r}\right), \tag{15.4}$$

with r_c the radius where the island size stays constant under the given parameters. For $\kappa = 1$, $a/\kappa r$ is small compared with $\ln(R/r)$, and one finds Eq. (15.3) in its large r-limit. Ostwald ripening for Si(100) surfaces showed attachment barriers (Theis et al., 1995) related to the fact that attachment to a Si(100) step requires concerted motion of two neighboring Si-dimers (Pearson et al., 1995). In the limit $r \ll r_c$, Eq. (15.4) predicts a scaling exponent of $x = 1/2$ for $r(t)$, respectively, a linear decrease of $A(t)$.

Small Cu islands on Cu(100) have indeed been observed to linearly decay with time, and this independent of their environment (Hannon et al., 1997). Figure 15.8(a) shows 60 adatom islands on a large terrace, a situation where ripening is essentially local, i.e., the local coverage remains conserved and is redistributed between the islands. The size evolution of all islands, apart from one having undergone coalescence with another one, could perfectly be described by Eq. (15.4), whereas $\kappa = 0$ led to significant disagreement. The astonishing fact that a simple metal system exhibits significant attachment barriers for was attributed to ripening being dominated by vacancy and not by adatom motion (Hannon et al., 1997). Vacancy attachment has an additional barrier compared with vacancy
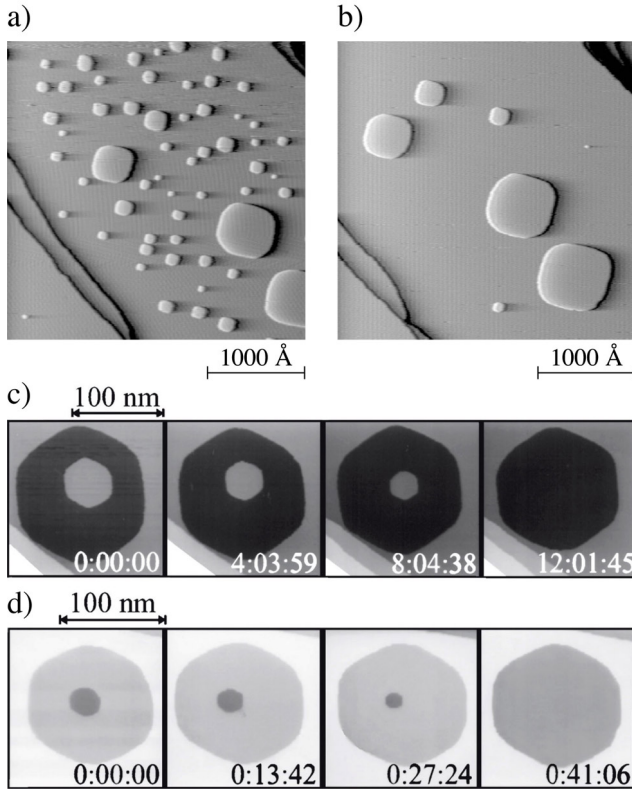
Fig. 15.8. (a) and (b) STM images showing ripening of an assembly of about 60 Cu adatom islands on Cu(100). 5 h 33 min have passed between left and right figure with the substrate held at 343 K (Hannon et al., 1997). The time- and temperature-dependent decay of Ag adatom (c) and vacancy islands (d) placed into vacancy islands on Ag(111) permits determination of the activation barrier of atom detachment from steps, and of the additional barrier for descending a step ((c) $T = 300$ K, (d) $T = 360$ K) (Morgenstern et al., 1998).

diffusion since it requires motion of two atoms. Vacancy motion has been confirmed for this system by tracing the displacement of In atoms on Cu(100) (Gastel et al., 2001).

An experiment with well defined boundary conditions has been conducted for Ag/Ag(111) (Morgenstern et al., 1998). Studying the decay dynamics of adatom (see Fig. 15.8(c)) and vacancy islands (see Fig. 15.8(d)) within a big vacancy island has the advantage of eliminating less well defined parameters, such as R. The decay of an adatom island of radius r within a vacancy island of radius R is given by

$$A(t, T) = -\beta \frac{e^{\gamma/k_B T n r} - e^{-\gamma/k_B T n R}}{a/r + \ln(R/r) + a/R}.$$
(15.5)

The authors first deduced $\gamma = 0.75 \pm 0.15$ eV/nm from fitting decay rates of three adatom and four vacancy islands. The island area $A(t, T)$ showed Arrhenius behavior from 240 to 310 K for $\beta = 2\pi D\rho_\infty/n$, highlighting the role of D in this term. With $\beta \propto \nu_0 e^{-E_E/k_B T}$ the authors found the energy barrier and attempt frequency for atom detachment from

steps onto terraces (diffusion barrier + binding E difference between kink and terrace site) $E_E = 0.71 \pm 0.03$ eV and $\nu_0 = 10^{12\pm0.6}$ Hz. For the geometry shown in Fig. 15.8(d), the filling and hence the decay of the small vacancy island is hindered by the Ehrlich–Schwöbel barrier for adatoms descending the step. This barrier is determined as $\Delta E_s = 0.13 \pm 0.04$ eV, consistent with former measurements reporting $\Delta E_s = 0.120 \pm 0.015$ eV, (Bromann et al., 1995).

Coarsening by Ostwald ripening is a means of preparing compact islands with narrow size distributions. The average size can be adjusted from $\langle s \rangle = 3$–10^3 atoms by varying the annealing temperature (Röder et al., 1993). This is of importance, since today much experimental and theoretical effort focuses on exploring the evolution of chemical and physical properties of small agglomerates of matter as a function of the number of atoms they contain (Jena et al., 1992; Gambardella et al., 2003).

The starting point for the controlled increase of mean cluster size by ripening is a large density of small clusters, mostly dimers, which are prepared by deposition of 0.1 ML at a temperature chosen such that there is little mobility in the time of deposition ($D/F < 10^3$, where D is the diffusion coefficient and F the deposition flux). In this post-nucleation regime monomers diffuse towards each other after deposition leading to a mean cluster size of $\langle s \rangle \sim 3$ atoms (Müller et al., 1996; Brune et al., 1999). The same result is obtained when depositing at temperatures where diffusion is frozen and subsequently gently annealing the surface to activate diffusion. After preparation of the small clusters, their densities are monitored by STM as a function of annealing temperature. This yields the average size since the coverage θ is a known constant.

The Ag islands on Pt(111) shown in Fig. 15.9(a) contain on average 14 atoms and are compact spherical. In Fig. 15.9(b) they contain 200 atoms and adopt a quasi-hexagonal shape. The largest ones clearly show the different lengths of the **A**- and **B**-type facets, corresponding to (110)– and (111)–micro-facets with lower surface energy for the latter. This shape becomes even more evident upon annealing to 280 K ($\langle s \rangle = 800$ atoms, not shown) and can be considered as the equilibrium shape of a 2D cluster for that system since further annealing leads to island decay, which is believed to be promoted by compressive stress resulting from the lattice mismatch between Ag and Pt (Blandin et al., 1994; Röder et al., 1994).

The evolution of the mean size $\langle s \rangle$ as function of the annealing temperature shows a plateau followed by an exponential increase, characteristic of Ostwald ripening (see Fig. 15.9(c)). The constant regime implies that the most fragile objects in the population, namely the dimers (and on square lattices also the trimers), neither dissociate nor diffuse, since both would lead to coarsening. The temperature threshold for the onset of 2D Ostwald ripening thus defines the $i = 1$ regime, where monomers are critical and dimers stable clusters, and yields the dimer bond energy $E_b = 150 \pm 20$ meV under the assumption $E_{diss} = E_m + E_b$ (Brune et al., 1999).

As an advantage to island nucleation, the size distributions obtained from Ostwald ripening are significantly sharper. This becomes evident from inspection of the STM images in Figs. 15.9(a) and (b) and from the size distribution shown in Fig. 15.9(d). The half width at half maximum decreases from $\sigma = 0.55$ for regular $i = 1$ nucleation to $\sigma = 0.30$ for coarsening. This is wider than $\sigma = 0.20$ reported for nucleation on a periodic template and much wider than the theoretical limit of $\sigma = 0.04$ predicted for that
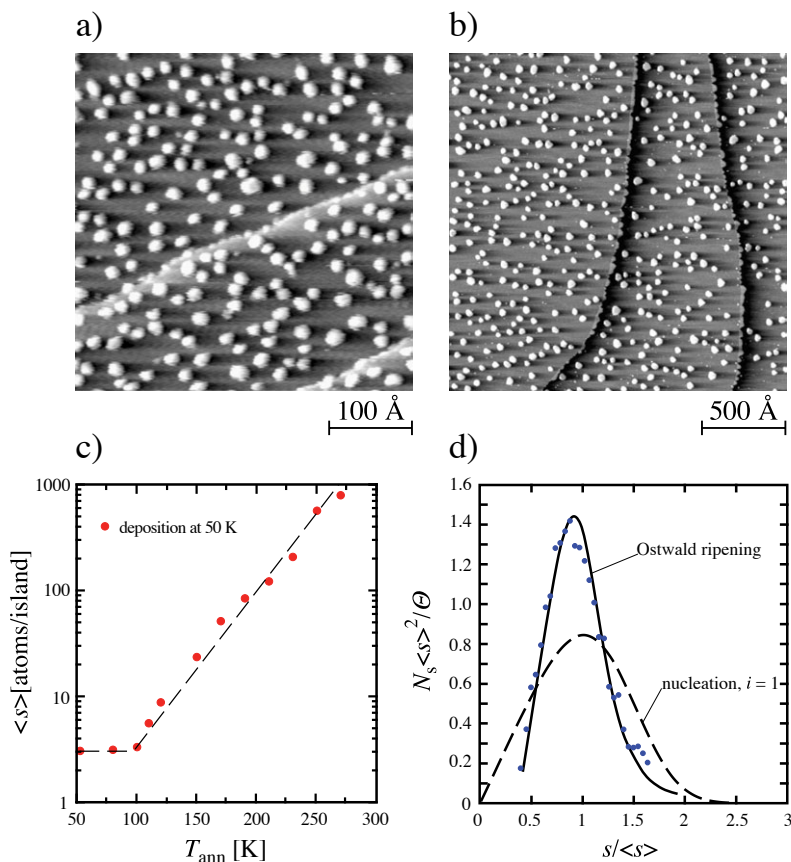
Fig. 15.9. (a) and (b) STM images of Ostwald ripening for Ag/Pt(111) creating compact 2D islands with their mean size $\langle s \rangle$ controlled by the annealing temperature (deposition of $\Theta = 0.10$ ML at 50 K creates $\langle s \rangle = 2.5$ atoms, (a) $T_{ann} = 140$ K, $\langle s \rangle = 14$ atoms, (b) $T_{ann} = 230$ K, $\langle s \rangle = 200$ atoms) (Röder et al., 1993). (c) $\langle s \rangle$ stays constant until $T_{ann} = 100$ K, from where on it exhibits an exponential increase. (d) Island size distributions for Ostwald ripening collapse with the used normalization into a single curve for all annealing temperatures and are significantly more narrow than nucleation (solid line guide to the eye, dashed line theoretical $i = 1$ scaling curve (Amar and Family, 1995)) (Brune, 2000).

case (Brune et al., 1998). However, Ostwald ripening is also significantly simpler as it works on a homogeneous substrate. Similar to nucleation, the island size distributions obtained from Ostwald ripening at various temperatures (Brune, 1998) become congruent when scaled the same way as for nucleation. We finally note that for systems with high cohesive energy, such as Co, Fe, and Pt on Pt(111), annealing of monomers leads to cluster diffusion rather than dissociation (Rusponi et al., 2008). Every cluster size has its characteristic onset-temperature of diffusion giving rise to a staircase increase of the mean island size.
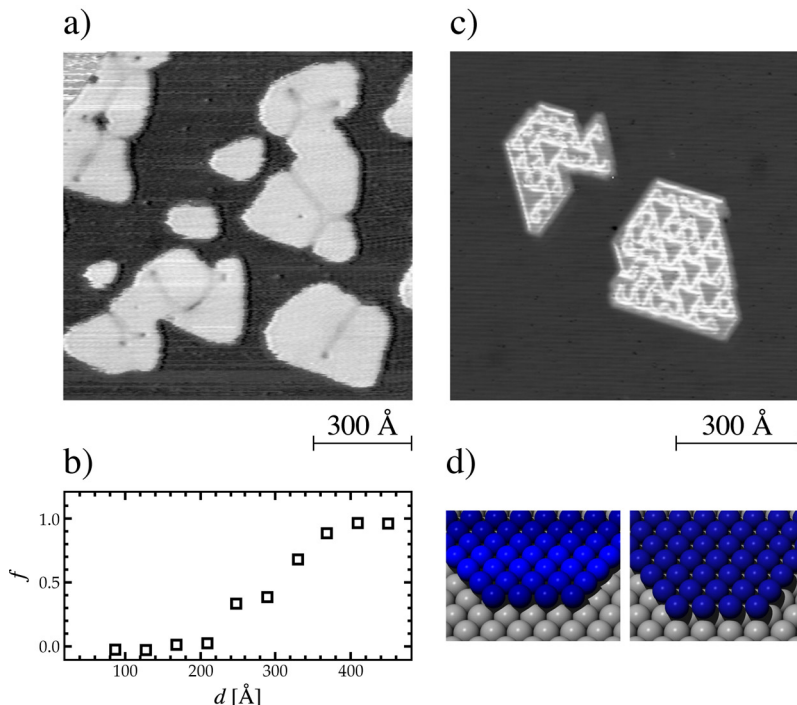
Fig. 15.10. (a) Ag monolayer islands on Pt(111). Small islands are pseudomorphic while from a critical size of 300 Å on (b) partial dislocations relieve the compressive stress resulting from the misfit of 4.2% (Bromann et al., 1997). ($\Theta = 0.12$ ML at $T_{dep} = 50$ K, Ostwald ripening at $T_{ann} = 300$ K, subsequent deposition of $\Theta = 0.25$ ML at 300 K.) (c) STM image of Co monolayer islands on Pt(111) showing a network of surface partials appearing bright and separating hcp from hcp stacking areas. **A**-steps have a partial dislocation in front while **B**-steps do not. (d) Ball model showing how **A**-steps (right) transform into **B**-steps (left) by a partial dislocation running parallel to the step (Cren et al., 2004).

15.6. Stress relief in monolayer islands

We briefly discuss how stress due to lattice mismatch and low coordination is relieved in islands compared with surfaces. Single crystal surfaces are under tensile stress due to missing bonds of the surface atoms. This gives rise to reconstructions, even for close-packed surfaces (Barth et al., 1990; Bott et al., 1993). In heteroepitaxy an additional contribution to surface stress is the misfit between the adsorbate and the substrate. Upon reaching a critical value, stress is relieved in thin films by partial dislocations (Brune et al., 1994) or by moiré patterns (Günther et al., 1995). In islands, stress relief can take place at their steps. As a consequence, the critical island size before introduction of partial dislocations can be much larger than the average distance between dislocations in continuous thin films (Bromann et al., 1997). This is illustrated in Fig. 15.10(a) which shows fully pseudomorphic Ag islands on Pt(111) coexisting with larger islands with partial surface dislocations inside. The critical diameter for the introduction of dislocations is inferred to 300 Å from the fraction f of islands having dislocations as a function of their diameter d, see Fig. 15.10(b). This value is notably

larger than the dislocation distance of 70 Å in a continuous film (Bromann et al., 1997; Hamilton et al., 1999).

For Co on Pt(111) stress is relieved by a network of partial dislocations visible as bright lines in the STM image Fig. 15.10(c). On close-packed surfaces there are two types of straight steps turned by 60° with respect to each other. One is a close-packed (111)-facet and called **B**-step, while the other is the energetically more costly because more open (110)-facet and called **A**-step. This gives rise to quasi-hexagons as island equilibrium shapes, where the length of the respective step segment gives access to its surface free energy (see Fig. 15.11(b) below). In Fig. 15.10(c) one sees that at one step-type there is a partial dislocation running parallel to the step in its immediate vicinity, whereas this feature is absent for the other step-type. The ones with partial dislocations are the **A**-steps, which are transformed by the stacking fault from fcc to hcp into the energetically favored **B**-steps, see ball model in Fig. 15.10(d). Thus the islands are entirely bound by (111)-facets which reduces the perimeter energy.

15.7. Bimetallic core-shell islands

Low-coordinated atoms play a key role in heterogeneous catalysis (Ertl and Freund, 1999) and magnetism (Billas et al., 1994). One illustration from catalysis is the barrier decrease of N_2-dissociation on Ru(0001) going from $E_{\mathrm{diss,terr}} = 1.3 \pm 0.2$ eV at terraces to $E_{\mathrm{diss,step}} = 0.4 \pm 0.1$ eV at steps, leading to a reduction of the sticking coefficient by seven orders of magnitude upon step passivation with Au (Dahl et al., 1999) (see also (Vang et al., 2005)). An example in the field of magnetism is the observation that step decoration of a thin Co film with Cu turns its easy magnetization axis by 90° from parallel to perpendicular to the steps (Weber et al., 1995).

A more recent discovery was that step atoms determine the magnetic anisotropy energy K of mono- and bilayer Co islands on a Pt(111) surface (Rusponi et al., 2003). The step atoms contribute with $K = 0.9 \pm 0.1$ meV to the overall anisotropy of the island, whereas the 6-fold coordinated surface atoms had a magnetocrystalline anisotropy close to the 20 times smaller Co bulk value of $K = 0.045$ meV/atom. This strong coordination effect was observed to continue to single adsorbed atoms (Gambardella et al., 2003). Heptamers had $K = 1.0 \pm 0.1$ meV/atom, which confirms the step result since six out of the seven atoms are step atoms, and monomers had $K = 9 \pm 1$ meV. As a consequence, single atoms are more stable magnets than clusters containing seven atoms, fractal islands are harder magnets than compact ones due to their for a given area longer perimeter, and finally the anisotropy can be adjusted independently from the magnetic moment in core-shell islands. Putting an element with low anisotropy at the edge and an element with high moment in the middle of the island produces soft magnets with high moments and therefore very low switching fields. On the other hand, hard elements at the border and nonmagnetic elements in the middle increase the islands anisotropy while minimizing its overall magnetic moment.

For many elements the preparation of bi-metallic core-shell islands is non-trivial due to the tendency of insertion into the substrate or core, and the Ehrlich–Schwöbel barrier
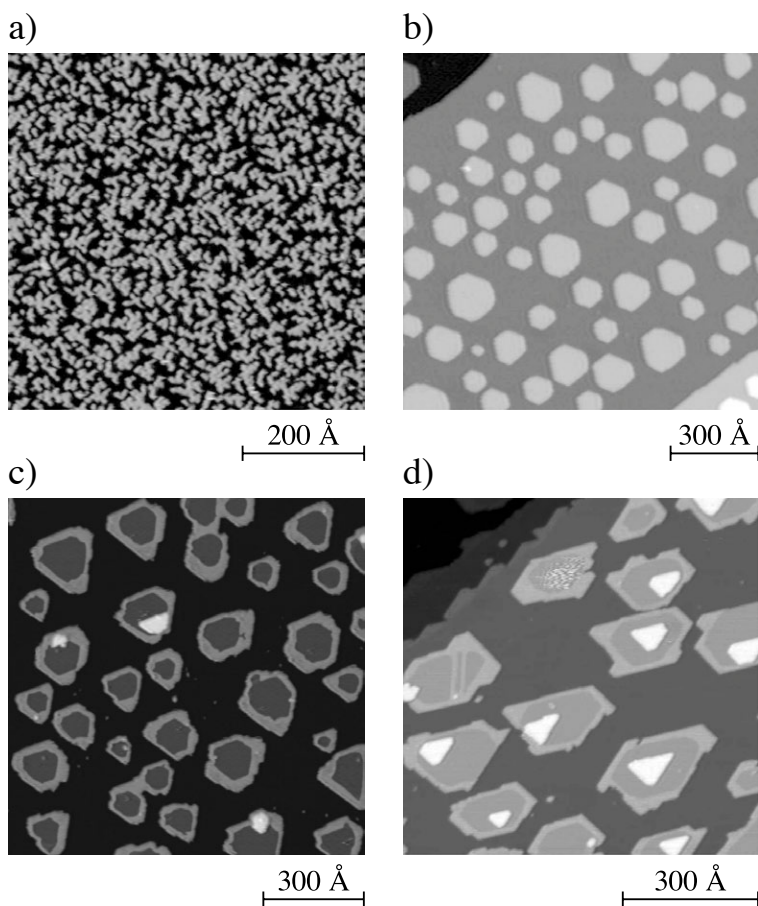
a)

b)

200 Å

c)

d)

300 Å

300 Å

300 Å

Fig. 15.11. STM images illustrating the growth steps for the creation of islands with a Pt core surrounded by a Co rim. (a) Pt deposition at 130 K produces small fractal islands ($\Theta = 0.40$ ML). (b) Annealing to $T_{ann} = 770$ K transforms fractal islands into larger quasi hexagons ($\Theta = 0.25$ ML, $T_{dep} = 170$ K). (c) Co deposition at 220 K allows to decorate the Pt cores with thin Co rims ($\Theta_{Co} = 0.15$ ML). (d) Co deposition at slightly too high temperatures and on too large Pt cores causes Co insertion into Pt (see pair of dislocations on one Pt island) and second layer growth ($T_{dep,Pt} = 240$ K, $T_{ann} = 790$ K, $T_{dep,Co} = 250$ K) (Weiss, 2004).

inhibiting descent of the shell element arriving on the core. An example for islands with a Pt core and a Co rim on Pt(111) is illustrated in Fig. 15.11.

The desired density and size of the core are defined by the deposition temperature and coverage, respectively. At the experimental deposition flux of $F = 0.02$ ML/min Pt/Pt(111) forms the desired density of $n_x = 2.5 \times 10^{-4}$ islands/unit cell at $T_{dep} = 200$ K, as inferred from inserting the diffusion barrier and pre-exponential factor of that system (Bott et al., 1996; Kyuno et al., 1998) into the scaling laws of nucleation (Brune et al., 1999). Limited mobility along steps gives rise to fractal island shapes for that system up to $T_{dep} = 400$ K (Michely et al., 1993), see also Fig. 15.11(a). In order to get a compact

core the islands have to be annealed. This also leads to coarsening implying a slightly lower deposition temperature for the first step. The ideal parameters for Pt/Pt(111) are deposition at 170 K, followed by annealing at 770 K leading to compact monolayer Pt islands with a quasi-hexagonal thermodynamic equilibrium shape (Michely et al., 1993), see Fig. 15.11(b).

A two to three atoms wide rim is created around the Pt core by deposition of 0.15 ML Co at 220 K, see Fig. 15.11(c). In the STM images, Co and Pt can be discerned by their apparent height difference of about 0.3 Å. The Co deposition temperature has to be chosen high enough to inhibit nucleation of Co islands between and on-top of Pt islands. The first requirement is less stringent, one readily achieves $n_{x,Co} \ll n_{Pt\text{-}core}$, while the second requirement is in conflict with Co insertion into the Pt(111) surface starting at 180 K. The probability of second layer nucleation is essentially given by the Ehrlich–Schwöbel barrier (Bromann et al., 1995; Rottler and Maass, 1999; Heinrichs et al., 2000) and has to be sufficiently low. Co insertion in the presence of Pt adatom islands takes place at slightly higher temperatures since the islands reduce the tensile stress of the Pt(111) surface. The temperature range constituting the best compromise between avoiding insertion and second layer nucleation is for the present system $200 \text{ K} \leqslant T_{dep,Co} \leqslant 260 \text{ K}$. Figure 15.11(c) shows that Co islands only occasionally grow on-top of the biggest Pt islands. The size of the Pt core and the deposition temperature are quite critical as illustrated in Fig. 15.11(d). Insertion of Co in the Pt core took place at one island on the left, as evidenced by the pair of parallel partial dislocations imaged bright. In addition, almost on all the cores small second layer nuclei can be observed.

15.8. Conclusions

The examples discussed in this chapter shed light onto the very early stage of metal on metal growth and on its use for the preparation of atomic superlattices or of small two-dimensional islands with well defined size, shape and distance. Also Ostwald ripening and the preparation of bimetallic islands with a core-shell structure have been discussed. These islands are particularly well suited for the investigation of interface and coordination effects. As to what magnetic properties are concerned, such effects are stronger than formerly anticipated. The systems discussed are meant to be examples for metal on metal systems, and the techniques discussed can also be applied to metals on oxide and semiconductor surfaces.

Acknowledgement

References

Amar, J.G., Family, F., 1995. Phys. Rev. Lett. 74, 2066.

Barth, J.V., Brune, H., Ertl, G., Behm, R.J., 1990. Phys. Rev. B 42, 9307.

Barth, J.V., Brune, H., Fischer, B., Weckesser, J., Kern, K., 2000. Phys. Rev. Lett. 84, 1732–1735.

Bauer, E., Poppa, H., Todd, G., Bonczek, F., 1974. J. Appl. Phys. 45, 5164.

Billas, I.M.L., Châtelain, A., Heer, W.A.d., 1994. Science 265, 1682.

Blandin, P., Massobrio, C., Ballone, P., 1994. Phys. Rev. Lett. 72, 3072.

Bogicevic, A., Ovesson, S., Hyldgaard, P., Lundqvist, B.I., Brune, H., Jennison, D.R., 2000. Phys. Rev. Lett. 85, 1910.

Borroni-Bird, C.E., Al-Sarraf, N., Andersson, S., King, D.A., 1991. Chem. Phys. Lett. 183, 516.

Bott, M., Hohage, M., Michely, T., Comsa, G., 1993. Phys. Rev. Lett. 70, 1489.

Bott, M., Hohage, M., Morgenstern, M., Michely, T., Comsa, G., 1996. Phys. Rev. Lett. 76, 1304.

Bromann, K., Brune, H., Giovannini, M., Kern, K., 1997. Surf. Sci. 388, L1107.

Bromann, K., Brune, H., Röder, H., Kern, K., 1995. Phys. Rev. Lett. 75, 677.

Brown, W.A., Kose, R., King, D.A., 1998. Chem. Rev. 98, 797.

Brune, H., 1998. Surf. Sci. Rep. 31, 121.

Brune, H., 2000. Growth of metal clusters at surfaces. In: Meiwes-Broer, K.H. (Ed.), Metal Clusters at Surfaces. Springer Series in Cluster Physics. Springer, Berlin, p. 67.

Brune, H., 2001. Metals on metals. In: Bonzel, H.P. (Ed.), Physics of Covered Solid Surfaces. In: Landolt Börnstein New Series, Group III: Condensed Matter, vol. 42. Springer, Berlin, p. 217. Subvolume A, Part 1.

Brune, H., 2006. Superlattices of atoms, molecules, and islands. In: Rosei, F., Grütter, P., Hofer, W. (Eds.), Properties of Single Organic Molecules on Crystal Surfaces. Springer, New York, pp. 247–267.

Brune, H., Bales, G.S., Boragno, C., Jacobsen, J., Kern, K., 1999. Phys. Rev. B 60, 5991.

Brune, H., Bromann, K., Röder, H., Kern, K., Jacobsen, J., Stoltze, P., Jacobsen, K., Nørskov, J., 1995. Phys. Rev. B 52, 14380. R.

Brune, H., Giovannini, M., Bromann, K., Kern, K., 1998. Nature 394, 451.

Brune, H., Röder, H., Boragno, C., Kern, K., 1994. Phys. Rev. B 49, 2997.

Brune, H., Wintterlin, J., Ertl, G., Behm, R.J., 1990. Europhys. Lett. 13, 123.

Chakraverty, B.K., 1967. J. Phys. Chem. Solids 28, 2401.

Christensen, A., Ruban, A.V., Stoltze, P., Jacobsen, K.W., Skriver, H.L., Nørskov, J.K., Besenbacher, F., 1997. Phys. Rev. B 56, 5822.

Cren, T., Rusponi, S., Weiss, N., Epple, M., Brune, H., 2004. J. Phys. Chem. B 108, 14685.

Crommie, M.F., Lutz, C.P., Eigler, D.M., 1993a. Nature 363, 524.

Crommie, M.F., Lutz, C.P., Eigler, D.M., 1993b. Science 262, 218.

Dahl, S., Logadottir, A., Egeberg, R.C., Larsen, J.H., Chorkendorff, I., Törnqvist, E., Nørskov, J.K., 1999. Phys. Rev. Lett. 83, 1814.

Egelhoff, W.F., Jacob, I., 1989. Phys. Rev. Lett. 62, 921.

Ehrlich, G., 1964. Brit. J. Appl. Phys. 15, 349.

Ehrlich, G., Watanabe, F., 1991. Langmuir 7, 2555.

Ertl, G., Freund, H.J., 1999. Physics Today 52, 32.

Evans, J.W., Sanders, D.E., Thiel, P.A., DePristo, A.E., 1990. Phys. Rev. B 41, 5410.

Evans, J.W., Thiel, P.A., Bartelt, M.C., 2006. Surf. Sci. Rep. 61, 1–128.

Feibelman, P.J., Nelson, J.S., Kellogg, G.L., 1994. Phys. Rev. B 49, 10548.

Fichthorn, K.A., Merrick, M.L., Scheffler, M., 2002. A kinetic Monte Carlo investigation of island nucleation and growth in thin-film epitaxy in the presence of substrate-mediated interactions. Appl. Phys. A 75, 17.

Fichthorn, K.A., Merrick, M.L., Scheffler, M., 2003. Nanostructures at surfaces from substrate-mediated interactions. Phys. Rev. B 68, 041404.

Fichthorn, K.A., Scheffler, M., 2000. Phys. Rev. Lett. 84, 5371.

Fischer, B., Brune, H., Fricke, A., Barth, J.V., Kern, K., 1999. Phys. Rev. Lett. 82, 1732.

Friedel, J., 1958. Nuovo Cimento Suppl. 7, 287–311.

Gambardella, P., Rusponi, S., Veronese, M., Dhesi, S.S., Grazioli, C., Dallmeyer, A., Cabria, I., Zeller, R., Dederichs, P.H., Kern, K., Carbone, C., Brune, H., 2003. Science 300, 1130.

Gastel, R.v., Somfai, E., Albada, S.B.v., Saarloos, W.v., Frenken, J.W.M., 2001. Phys. Rev. Lett. 86, 1562.

Gölzhäuser, A., Ehrlich, G., 1996. Phys. Rev. Lett. 77, 1334.

Günther, C., Vrijmoeth, J., Hwang, R.Q., Behm, R.J., 1995. Phys. Rev. Lett. 74, 754.

Günther, S., Hitzke, A., Behm, R.J., 1997. Surf. Rev. Lett. 4, 1103.

Gurney, T., Hutchinson, F., Young, R.D., 1965. J. Chem. Phys. 42, 3939.

Habenschaden, E., Küppers, J., 1984. Surf. Sci. 138, L147.

Hamilton, J.C., Stumpf, R., Bromann, K., Giovannini, M., Kern, K., Brune, H., 1999. Phys. Rev. Lett. 82, 4488.

Hannon, J.B., Klünker, C., Giesen, M., Ibach, H., Bartelt, N.C., Hamilton, J.C., 1997. Phys. Rev. Lett. 79, 2506.

Hansen, M., 1958. Constitution of Binary Alloys. Mc Graw Hill, New York, Toronto, London.

Hasegawa, Y., Avouris, P., 1993. Phys. Rev. Lett. 71, 1071.

Heinrichs, S., Rottler, J., Maass, P., 2000. Phys. Rev. B 62, 8338.

Hitzke, A., Hugenschmidt, M.B., Behm, R.J., 1997. Surf. Sci. 389, 8.

Hofer, W.A., Garcia-Lekue, A., Brune, H., 2004. Chem. Phys. Lett. 397, 354.

Hyldgaard, P., Persson, M., 2000. J. Phys.-Condens. Mat. 12, L13.

Jeandupeux, O., Bürgi, L., Hirstein, A., Brune, H., Kern, K., 1999. Phys. Rev. B 59, 15926.

Jena, P., Khanna, S.N., Rao, B.K. (Eds.), 1992. Physics and Chemistry of Finite Systems: From Clusters to Crystals. Kluwer, Dordrecht.

Kellogg, G.L., 1996. Phys. Rev. Lett. 76, 98.

Kittel, C., 1986. Introduction to Solid State Physics. John Wiley & Sons, New York.

Knorr, N., Brune, H., Epple, M., Hirstein, A., Schneider, A.M., Kern, K., 2002. Phys. Rev. B 65, 115420.

Koh, S.J., Ehrlich, G., 2001. Phys. Rev. Lett. 87, 106103.

Kolaczkiewicz, J., Bauer, E., 1986. Surf. Sci. 175, 508.

Kyuno, K., Gölzhäuser, A., Ehrlich, G., 1998. Surf. Sci. 397, 191.

Lau, K.H., Kohn, W., 1977. Surf. Sci. 65, 607.

Lau, K.H., Kohn, W., 1978. Surf. Sci. 75, 69.

Lifshitz, L.M., Slyozov, V.V., 1961. J. Phys. Chem. Solids 19, 35.

Liu, C., Yamazaki, S., Hobara, R., Matsuda, I., Hasegawa, S., 2005. Phys. Rev. B 71, 041310.

Michely, T., Hohage, M., Bott, M., Comsa, G., 1993. Phys. Rev. Lett. 70, 3943.

Michely, T., Krug, J., 2004. Islands, Mounds, and Atoms. Springer Series in Surface Sciences, vol. 42. Springer, Berlin.

Morgenstern, K., Rosenfeld, G., Comsa, G., 1996. Phys. Rev. Lett. 76, 2113.

Morgenstern, K., Rosenfeld, G., Lægsgaard, E., Besenbacher, F., Comsa, G., 1998. Phys. Rev. Lett. 80, 556.

Müller, B., Fischer, B., Nedelmann, L., Brune, H., Kern, K., 1996. Phys. Rev. B 54, 17858.

Nyberg, G.L., Kief, M.T., Egelhoff, W.F., 1993. Phys. Rev. B 48, 14509.

Ostwald, W., 1900. Z. Phys. Chem. 34, 495.

Ovesson, S., Bogicevic, A., Wahnström, G., Lundqvist, B.I., 2001. Phys. Rev. B 64, 125423.

Pearson, C., Krueger, M., Ganz, E., 1995. Phys. Rev. Lett. 74, 2710.

Repp, J., Moresco, F., Meyer, G., Rieder, K.H., Hyldgaard, P., Persson, M., 2000. Phys. Rev. Lett. 85, 2981.

Röder, H., Brune, H., Kern, K., 1994. Phys. Rev. Lett. 73, 2143.

Röder, H., Hahn, E., Brune, H., Bucher, J.P., Kern, K., 1993. Nature 366, 141.

Rottler, J., Maass, P., 1999. Phys. Rev. Lett. 83, 3490.

Rusponi, S., Cren, T., Longwitz, S.R., Lehnert, A., Moulas, G., Buluschek, P., Goyhenex, C., Vargoz, E., Kern, K., Brune, H., 2008. Unpublished.

Rusponi, S., Cren, T., Weiss, N., Epple, M., Buluschek, P., Claude, L., Brune, H., 2003. Nat. Mater. 2, 546.

Sanders, D.E., DePristo, A.E., 1991. Surf. Sci. 254, 341.

Silly, F., Pivetta, M., Ternes, M., Patthey, F., Pelz, J.P., Schneider, W.D., 2004a. Phys. Rev. Lett. 92, 016101.

Silly, F., Pivetta, M., Ternes, M., Patthey, F., Pelz, J.P., Schneider, W.D., 2004b. N. J. Phys. 6, 16.

Stepanyuk, V.S., Baranov, A.N., Tsivlin, D.V., Hergert, W., Bruno, P., Knorr, N., Schneider, M.A., Kern, K., 2003. Phys. Rev. B 68, 205410.

Stepanyuk, V.S., Negulyaev, N.N., Niebergall, L., Longo, R.C., Bruno, P., 2006. Phys. Rev. Lett. 97, 186403.

Stepanyuk, V.S., Niebergall, L., Longo, R.C., Hergert, W., Bruno, P., 2004. Phys. Rev. B 70, 075414.

Stranick, S.J., Kamna, M.M., Weiss, P.S., 1994. Science 266, 99.

Stroscio, J.A., Celotta, R.J., 2004. Science 306, 242.

Stuckless, J.T., Starr, D.E., Bald, D.J., Campbell, C.T.J., 1997. Chem. Phys. 107, 5547.

Sykes, M.F., Gaunt, D.S., Glen, M., 1976. J. Phys. A. Math. Gen. 9, 97.

Sykes, M.F., Glen, M., 1976. J. Phys. A. Math. Gen. 9, 87.

Theis, W., Bartelt, N.C., Tromp, R.M., 1995. Phys. Rev. Lett. 75, 3328.

Trost, J., Zambelli, T., Wintterlin, J., Ertl, G., 1996. Phys. Rev. B 54, 17850.

Tsivlin, D.V., Stepanyuk, V.S., Hergert, W., Kirschner, J., 2003. Phys. Rev. B 68, 205411.

Tsong, T.T., 1988. Rep. Prog. Phys. 51, 759.

Vandoni, G., Félix, C., Monot, R., Buttet, J., Harbich, W., 1994. Surf. Sci. 320, L63.

Vang, R.T., Honkala, K., Dahl, S., Vestergaard, E.K., Schnadt, J., Lægsgaard, E., Clausen, B.S., Nørskov, J.K., Besenbacher, F., 2005. Nat. Mater. 4, 160.

Venables, J.A., Brune, H., 2002. Phys. Rev. B 66, 195404.

Wagner, C., 1961. Z. Elektrochem. 65, 581.

Wahlström, E., Ekvall, I., Olin, H., Walldén, L., 1998. Appl. Phys. A 66, S1107.

Wang, S.C., Ehrlich, G., 1989. Phys. Rev. Lett. 62, 2297.

Wang, S.C., Ehrlich, G., 1990. Surf. Sci. 239, 301.

Wang, S.C., Ehrlich, G., 1991. J. Chem. Phys. 94, 4071.

Wang, S.C., Ehrlich, G., 1993a. Phys. Rev. Lett. 70, 41.

Wang, S.C., Ehrlich, G., 1993b. Phys. Rev. Lett. 71, 4174.

Weber, W., Back, C.H., Bischof, A., Pescia, D., Allenspach, R., 1995. Nature 374, 788.

Weiss, N., 2004. Propriétés magnétiques de nanostructures de cobalt adsorbées. Ph.D. thesis, EPFL.

Weiss, P.S., Eigler, D.M., 1992. Phys. Rev. Lett. 69, 2240.

Wintterlin, J., Wiechers, J., Brune, H., Gritsch, T., Höfer, H., Behm, R., 1989. Phys. Rev. Lett. 62, 59.

Wynblatt, P., Gjostein, N.A., 1975. Pergamon, Oxford. p. 21, vol. 9.

Yayon, Y., Lu, X.H., Crommie, M.F., 2006. Phys. Rev. B 73, 155401.

Young, R.D., Schubert, D.S., 1965. J. Chem. Phys. 42, 3943.